

SUPPLEMENTAL TEXT AND FIGURES

Hydrogen Generation and Iron Partitioning During Experimental Serpentinization of an Olivine-Pyroxene Mixture

Thomas M. McCollom, Frieder Klein, Bruce Moskowitz, Thelma S. Berquó, Wolfgang Bach,
and Alexis Templeton

Contents:

S1. Detailed Methods

S2. Calculation of olivine dissolution rates at experimental conditions

Supplemental Tables S1-S5

Supplemental Figures S1-S14

S1. Detailed Methods

Analyses of dissolved H₂, total dissolved CO₂, CH₄, and C₂-C₆ hydrocarbons was performed using procedures described in detail in McCollom et al. (2001) and McCollom and Seewald (2001). Briefly, concentrations of total dissolved CO₂ ($\Sigma\text{CO}_2 = \text{CO}_{2(aq)} + \text{HCO}_3^- + \text{CO}_3^{2-}$) were determined by gas chromatography (GC) with thermoconductivity detection (TCD) following acidification of the sample with 25% phosphoric acid and extraction into a headspace with 1 ml He gas. Measured amounts of ΣCO_2 were corrected to account for the fraction remaining dissolved in the acidified fluid. Methane and hydrocarbons were analyzed on the same sample using Flame Ionization Detection (FID). Dissolved H₂ was analyzed by GC with thermoconductivity detection (TCD) following a headspace extraction.

To account for differences in fluid:rock ratios between experiments and changing amounts of fluid in the reaction cell over time as a result of sampling, the amount of H₂ generated was normalized by calculating the total number of moles of H₂ generated per gram of mineral reactants. For the calculations, the total amount of H₂ generated during each sample interval was determined by multiplying the change in dissolved H₂ concentration by the amount of fluid present in the reaction vessel at the time of sampling, and then dividing by the initial mass of minerals included in the experiments. To simplify the calculation, the small amounts of water incorporated into product minerals or converted to H₂ were neglected.

The pH_{25°C} was measured using a Ross micro combination electrode at room temperature with an uncertainty of approximately ± 0.1 units of the reported value. Dissolved SiO₂ was measured immediately after sampling with a Hach DR/2400 spectrophotometer using the heteropoly-blue method at a wavelength of 815 nm, with reagents and methods supplied by the manufacturer. An aliquot of the fluid was retained for analysis of major elements after dilution and acidification with a small amount of HNO₃, and subsequently analyzed for total dissolved Na, Ca, Mg, Fe, Si, and K by Inductively Coupled Plasma – Optical Emission Spectroscopy (ICP-OES). In almost all cases, the Si concentrations measured by ICP-OES were within 10% of SiO₂ values determined by spectrophotometry, so only the latter are reported here. At selected time points, fluid aliquots were analyzed for total dissolved chloride using titration against silver nitrate with chromate as an indicator.

Initial characterization of the morphology and chemical composition of solid reaction products was performed using a JEOL 6480LV Scanning Electron Microscope (SEM) equipped with an Oxford Instruments Electron-dispersive X-Ray Spectrometer (EDS) and INCA data processing software. Solids for SEM/EDS were examined both as uncoated grains mounted on Al stubs with carbon tape and as polished grain mounts embedded in epoxy and coated with carbon, using an accelerating voltage of 15 kV. Quantitative compositional data were obtained with Electron Microprobe Analysis (EMPA) using a JEOL JXA 8600 at the University of Colorado, which is equipped with five wavelength-dispersive spectrometers. Minerals were analyzed with an accelerating voltage of 15 kV for a beam current of 15-20 nA and a defocused 5 μm beam diameter. Both synthetic and natural mineral standards were used. Raw data were corrected using the CITZAF method (Armstrong, 1995). Owing to the small grain sizes and low abundance of reaction products, EMPA analyses were limited to a relatively small number of points in individual experiments. In addition, the small grain size and high porosity of the secondary products resulted in low wt% totals for many of the analyses, so measured compositions have relatively high uncertainties. However, the exact uncertainties are difficult to quantify.

Raman spectra of solid reaction products were obtained using a Horiba LabRAM HR confocal spectrometer equipped with a 17 mW 633 nm HeNe laser, an astigmatic flat field spectrograph

with a focal length of 800 mm, and a multichannel air-cooled (-70 °C) CCD detector. Individual spectra were recorded using a 40× long-distance objective. A grating with 600 grooves / mm and a confocal hole diameter of 100 to 200 μm was chosen for most analyses. Spectra were collected for 5 seconds with 3 accumulations between 100 cm⁻¹ and 1300 cm⁻¹ and between 3500 cm⁻¹ and 3800 cm⁻¹.

Mössbauer spectroscopy and magnetic investigations were carried out on powdered samples (~100 mg) at the Institute for Rock Magnetism (IRM), University of Minnesota, USA. Mössbauer spectra were measured at room temperature using a conventional constant-acceleration spectrometer in transmission geometry with a ⁵⁷Co/Rh source. An α-Fe foil at room temperature was used to calibrate isomer shifts and velocity scale. Mössbauer spectra were fit using the NORMOS program (Brand, 1987) providing estimates for isomer shift (IS) and quadrupole splitting (QS) for each subspectrum. Uncertainties for Mössbauer parameters are ±0.01 mm/s for IS and QS, and ±5% for spectral area. To focus on secondary products (primarily Fe in serpentine), they were physically separated from the bulk products by sonication with ethanol followed by removal of the suspended fraction. This procedure was repeated until the ethanol was no longer cloudy, and Mössbauer analysis performed on this prepared sample following evaporation of the ethanol. Magnetite was removed from products during this process using a strong magnet. Inspection of the remnant solids by SEM indicated that this method was effective in separating nearly all of the secondary silicates from unreacted primary minerals (see Supplemental Fig. S6).

Room temperature hysteresis loops were obtained in a vibrating sample magnetometer (Princeton Corporation Measurements) using an electromagnet to produce fields up to 1 T. Hysteresis parameters (saturation magnetization, M_s; saturation remanence, M_r; coercivity, B_c) were calculated after paramagnetic slope correction over the interval of 0.7-1.0 T using the non-linear approach-to-saturation fitting method of Jackson and Solheid [2010]. The magnetite weight-percent was determined from the room-temperature bulk saturation magnetization values and the known value for pure magnetite (M_s=92 Am²/kg) as follows:

$$\text{Magnetite weight percent} = \frac{M_s(\text{sample})}{M_s(\text{magnetite})} \times 100 \text{ percent} .$$

Low temperature remanent magnetization curves were obtained with a SQUID magnetometer (Quantum Design, San Diego, CA, USA – MPMS-XL). The data were obtained by cooling the sample to 10 K in a 2.5 T field (Field cooled (FC) magnetization). The field was then reduced to zero and the remanent magnetization was measured on warming to 300 K in 5 K steps.

Thermogravimetric analyses (TGA) were performed on the products of the experiments to determine the amount of hydrated minerals present, and these data were then used to estimate the amount of primary minerals reacted. The analyses were performed using a Netzsch STA 449 F3 Jupiter[®] thermoanalyzer at the University of Bremen. Finely ground samples (~100 mg) were weighed into an alumina crucible and heated from 30 °C to 1000 °C at 5 °C per minute while monitoring the change in mass. An empty crucible was measured as a blank value simultaneous with the sample to minimize errors in sample weighing during heating. Nitrogen (N₂) was used as the purge gas to avoid oxidation of Fe in the sample. The results show peak weight loss corresponding to dehydration of brucite at 320-370 °C, and of chrysotile at 600-650 °C (Viti, 2010).

The surface areas of the initial olivine reactants was measured using the conventional BET method with N₂ as the absorptive species, and was found to be 0.59 ± 0.02 m² g⁻¹. The surface area of Opx was not measured, but is likely to be similar to that of olivine for the grain size used (Brantley and Mellott, 2000). In any case, it should be borne in mind that owing to dissolution

and fracturing, the surface area of olivine and Opx steeply increase as the reactions proceed (e.g., Malvoisin et al., 2012b, 2017; McCollom et al., 2016), so the initial surface area probably has very limited relevance to the surface exposed to fluids during the course of the experiments.

S2. Reaction path model calculations

Reaction path models were carried out with EQ3/6 using the 350 bar database of McCollom and Bach (2009) with the addition of data for the cronstedtite endmember of the serpentine solid solution as described in Klein et al. (2013). Olivine and Opx were included in the model at the same relative proportions and fluid:rock ratio as in experiment OlivOpx230. A small amount of quartz (0.8 wt.% of total reactant minerals) and clinopyroxene (0.4 wt.%) were also added to represent contaminants present in the starting minerals. Because the initial fluid in EQ3/6 has a fixed mass of 1 kg, the mass of the starting minerals was scaled to achieve the same fluid:rock ratio as in the experiment, and then readjusted to the experimental amounts for display in the figures.

Since olivine and Opx may not have reacted at the same rate during the experiment, a series of models were constructed that varied the relative dissolution rates for these minerals. The relative rates here are defined on a gram-for-gram basis (i.e., the mass of each mineral dissolved during each increment of reaction progress), so that the overall flux of elements contributed by dissolution of individual minerals during each increment of reaction progress depends on both the relative dissolution rate and the total mass of the reactant. As a consequence, even when Opx is constrained to dissolve more rapidly than olivine, olivine may contribute a greater total flux of elements to the reaction owing to its greater overall mass. For simplicity, the models assume that dissolution of olivine and Opx remains constant as a function of reaction progress; that is, the same mass of each mineral is dissolved during each increment in reaction progress until it is exhausted. Quartz and Cpx were constrained to completely dissolve during the early stages of the reaction path (i.e., first 2% of reaction progress).

Model results are portrayed here in terms of reaction progress, which is independent of any absolute time constraint. Selected experimental results from OlivOpx230 are also shown in the model diagrams to allow comparison with model results. Since the time required to achieve each increment of reaction progress may not remain constant during the reaction (for example, an increase in pH along the reaction path may result in a faster overall rate of serpentinization; McCollom et al., 2020), reaction progress may not be a linear function of time. More frequent sampling of the solid products along the reaction path than are available from the present experiments would be required to correlate reaction progress with absolute reaction rates.

In the absence of other constraints, data from OlivOpx230 are portrayed on the figures using the assumption that reaction progress was a linear function of reaction time, with the final measurement representing the point in reaction progress where 53% of the original reactants had been consumed. In reality, the extent of reaction progress was probably very slow prior the increase in pH and then accelerated following the increase. Thus, the experimental data points on the figures should probably be more compressed in the initial stages, and then spread farther apart during the latter half of the reaction.

A previous laboratory serpentinization study by Martin and Fyfe (1970) using individual minerals as reactants found that olivine reacted 3-5 times more rapidly than Opx in the temperature range of the OlivOpx230 experiment, and Okamoto et al. (2011) also reported that olivine reacted much more extensively than Opx in their experiments at 250 °C. In addition, olivine has been found to dissolve more rapidly than pyroxenes in laboratory dissolution experiments (e.g.,

Pokrovsky and Schott, 2000; Oelkers and Schott, 2001). Furthermore, previous reaction path models constructed to simulate serpentinization experiments have assumed olivine would react more rapidly than pyroxenes (e.g., Seyfried et al., 2007).

Accordingly, an initial reaction path model was constructed in which olivine was allowed to react three times faster than Opx (that is, each grain of olivine is assumed to react three times more rapidly than an equivalent grain of Opx). Results of this model are shown in Supplemental Fig. S11, where it can be seen that the model fails to reproduce critical features of the results from OlivOpx230. In particular, the model predicts that magnetite and brucite would begin precipitating at a very early stage in the reaction, which is contrary to the results of the shorter term experiments as well as the high SiO₂ levels observed in the early stages of OlivOpx230. The model also predicts that the Opx:olivine ratio among the remaining reactants should increase as the reaction progresses, with the proportion of Opx approaching 25% once 53 wt.% of the original minerals had reacted (i.e., the extent of reaction in OlivOpx230 based on TGA measurements; Table 4). This prediction is in clear disagreement with the absence of Opx in the experimental products. A model where olivine was allowed to react at the same rate as Opx similarly predicted that substantial amounts of Opx should have remained when OlivOpx230 was terminated (Supplemental Fig. S12), which was again contrary to the experimental results. The best fit to the experimental observations was achieved with a model where Opx was constrained to react two times as fast as olivine (see main text and Fig. 5).

Additional References Cited in Supplemental Text

- Armstrong, J. T. (1995) CITZAF: a package of correction programs for the quantitative electron microbeam X-ray analysis of thick polished materials, thin films, and particles. *Microbeam Anal.*, **4**,177–200.
- Brantley S. L. and Mellott N. P. (2000) Surface area and porosity of primary silicate minerals. *Am. Mineral.* **85**, 1767-1783.
- Dyar M. D., Agresti D. G., Schaefer M. W., Grant C. A., and Sklute E. C. (2006) Mossbauer spectroscopy of earth and planetary minerals. *Ann. Rev. Earth Planet. Sci.* **34**, 83-125.
- Jackson, M., and P. Solheid (2010), On the quantitative analysis and evaluation of magnetic hysteresis data. *Geochem. Geophys. Geosyst.*, 11(4), Q04Z15, doi: 10.1029/2009GC002932.
- Moskowitz B. M., Jackson M., and Kissel C. (1998). Low temperature magnetic behavior of titanomagnetites. *Earth Planet. Sci. Lett.*, **157**,141-149.

Supplemental Table S1. Fluid compositions measured during hydrothermal experiments.

Time (h)	Temp (°C)	H ₂ (m)	CO ₂ (m)	CH ₄ (μ)	Na (m)	Cl (m)	Si (m)	Fe (μ)	Mg (μ)	Ca (μ)	Al (μ)	K (μ)	pH (25°C)	pH in situ	H ₂ gen. [#] (μmol/g)	Fluid [†] (g)
<i>Experiment Opx230 (230 °C)</i>																
164	230	b.d.	19.5	38	-	-	1.6	-	-	-	-	-	7.5	-	0	45.8
476	230	0.001	18.9	39	496	-	1.8	10	b.d.	40	b.d.	b.d.	7.5	7.9	0.003	41.2
1030	230	0.002	21.1	42	494	-	1.8	b.d.	b.d.	66	b.d.	b.d.	7.2	7.9	0.004	37.9
1582	230	0.004	20.2	62	468	-	1.7	b.d.	b.d.	100	b.d.	b.d.	7.3	7.8	0.005	30.1
2348	230	0.004	20.5	39	479	488	1.9	b.d.	b.d.	160	b.d.	b.d.	6.9	7.8	0.005	
<i>Experiment OlivOpx230 (230 °C)</i>																
2	232	0.001	19.2	5.6	514	-	1.9	b.d.	b.d.	b.d.	b.d.	190	-	7.7	0	44.0
169	232	0.023	-	-	502	-	0.87	b.d.	300	70	b.d.	430	6.8	7.6	0.04	40.1
840	232	0.24	-	-	473	-	0.66	b.d.	12	52	b.d.	480	7.4	7.8	0.36	37.9
1344	232	0.39	-	-	524	-	0.55	b.d.	16	100	b.d.	490	7.0	7.7	0.59	34.2
2015	232	1.1	-	-	508	-	0.37	b.d.	b.d.	45	b.d.	490	7.4	7.8	1.5	32.0
3359	232	3.3	12.0	15.7	486	-	0.14	b.d.	b.d.	19	b.d.	540	8.1	7.9	4.1	29.1
4488	232	13.8	8.5	17.6	519	-	0.10	b.d.	b.d.	b.d.	b.d.	550	10.7	8.6	15.3	26.1
4511	232	-	-	-	-	500	-	-	-	-	-	-	-	-	-	-
4512	Additional fluid injected															
4535	232	6.1	9.0	8.4	536	-	0.046	b.d.	b.d.	b.d.	b.d.	250	9.5	8.2	15.3	43.5
5567	232	14.7	-	9.0	522	-	0.061	b.d.	b.d.	b.d.	b.d.	310	11.2	8.5	29.5	40.5
7271	232	35.8	-	17.	543	-	0.100	b.d.	b.d.	b.d.	20	350	11.6	8.8	60.5	36.0
8183	232	49.8	3.8	20.	528	-	0.063	b.d.	b.d.	b.d.	15	310	11.7	8.8	79.1	32.7
8711	232	52.0	3.3	22.	533	-	0.115	b.d.	b.d.	b.d.	14	300	11.7	8.8	81.9	29.2
9287	232	61.0	2.8	25.	537	500	0.090	b.d.	b.d.	b.d.	19	310	-	8.8	90.7	24.0
<i>Experiment OlivOpx230med (230 °C)</i>																
258	231	0.007	18.9	7.3	-	-	0.88	-	-	-	-	-	8.0	8.0	0.014	45.4
834	231	0.007	19.2	9.0	458	-	0.81	b.d.	b.d.	b.d.	b.d.	b.d.	7.7	7.9	0.016	41.7
1387	231	0.008	19.6	9.0	467	-	0.77	b.d.	b.d.	32	b.d.	b.d.	7.3	7.8	0.016	38.1
1939	231	0.008	17.6	9.1	458	-	0.71	b.d.	b.d.	62	b.d.	b.d.	6.9	7.7	0.014	34.5
2347	231	0.007	-	-	475	-	0.65	b.d.	b.d.	59	b.d.	b.d.	7.3	7.8	0.015	30.4
2709	231	0.008	14.9	8.8	456	464	0.66	b.d.	b.d.	69	b.d.	b.d.	7.2	7.8	0.016	27.3
<i>Experiment OlivOpx230short (230 °C)</i>																
19	231	b.d.	19.6	5.6	-	-	0.33	-	-	-	-	-	8.0	-	0	43.8
212	231	0.010	18.9	8.7	498	-	0.87	b.d.	b.d.	11	b.d.	220	7.8	7.9	0.02	40.3

379	231	0.017	18.3	9.3	498	-	0.86	b.d.	5	11	b.d.	240	7.6	7.9	0.03	36.4
620	231	0.020	18.9	9.9	500	500	0.91	b.d.	12	16	b.d.	240	7.6	7.9	0.03	32.7

Concentrations in mmol kg^{-1} (m) or $\mu\text{mol kg}^{-1}$ (μ). “b.d.” = below the detection limit of approximately 1 $\mu\text{mol/kg}$. “-“ = not measured. #Hydrogen generated per gram of reactant minerals. [†]Amount of fluid in reaction cell at time of sampling. Data for Harz230 at 3819 h following injection are estimated based on the composition of fluid prior to injection and the amount of fluid injected.

Supplemental Table S2. Predicted extent of reaction in OlivOPx230med based on reaction rates for olivine and Opx from experiments Oliv230 and Opx230.

Oliv230 duration	8183 h
% olivine reacted	4.9
Oliv230 olivine reaction rate	0.0006 %/h
Opx230 duration	2348 h
% olivine reacted	7.3
Opx230 Opx reaction rate	0.0031 %/h
OlivOpx230med duration	2709
Weight Opx in OlivOPx230med	3.2 g
Weight olivine in OlivOPx230med	18.0 g
Proportion Opx	0.15
Proportion olivine	0.85
Expected extent of Opx reaction in 2709 h	8.4%
Expected extent of olivine reaction in 2709 h	1.6%
Total expected extent of reaction in OlivOPx230med (mineral proportion times expected reaction)	2.6%
Extent of reaction in OlivOPx230med based on TGA	1.9%

Supplemental Table S3. Mass balance calculations to estimate the amount of H₂ that should have been generated from Fe^{III} incorporated into serpentine and magnetite in experiment OlivOpx230 and Oliv230pH from McCollom et al. (2020) .

	OlivOpx230	Oliv230pH
Weight initial reactants (g)	24.5	15.0
Approximate % reacted	53	70
Approximate % serpentine	49	64
Weight serpentine produced	12.0	9.6
Moles serpentine (assumes mol. wt. = 287 g)	0.042	0.033
Mg# serpentine	91	93
Moles Fe _{tot} in serpentine	0.011	0.0070
Percent Fe ^{III} of Fe _{tot} (from MB spectroscopy)	15	53
Moles Fe ^{III} in serpentine	0.0017	0.0037
Calculated moles H ₂ produced from serpentine	0.00085	0.0019
Calculated moles H ₂ produced from serpentine per g reactants	0.000035	0.00012
Wt% magnetite in products	1.52	1.6
Weight magnetite produced	0.40	0.264
Moles magnetite produced	0.0017	0.00114
Moles H ₂ produced from magnetite per g reactants	0.000069	0.000076
Total calculated moles H ₂ produced from serpentine and magnetite per g reactants	0.000104	0.00020
Observed moles H ₂ per g reactants	0.000091	0.000105
Fraction of H ₂ from serpentine	0.33	0.62
Fraction of H ₂ from magnetite	0.67	0.38

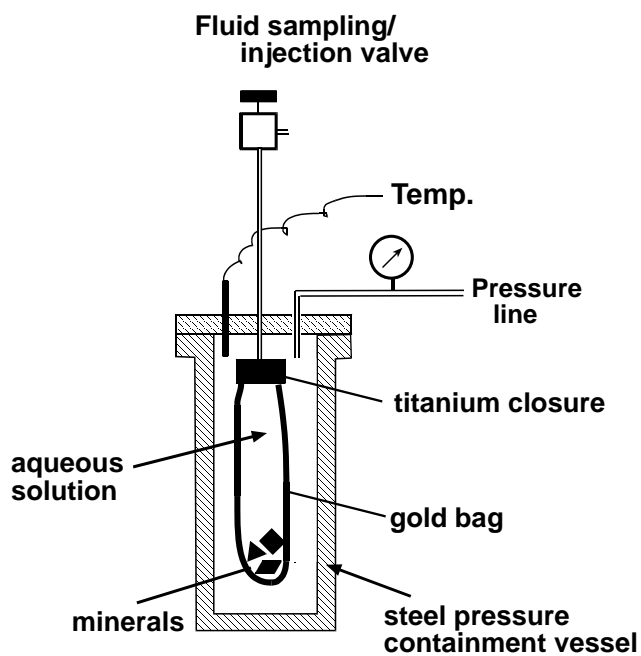
Supplemental Table S4. Calculated distribution of Fe among reaction products in experiment OlivOpx230 (all data given in mmoles per g total solids).

Mineral	Amount	Fe _{total}	Fe ^{II}	Fe ^{III}
Serpentine	1.78	0.480	0.408	0.072
Brucite	0.56	0.072	0.072	0
Magnetite	0.066	0.197	0.066	0.131
% Total Fe in products as Fe ^{III}			37	
% Fe ^{III} in magnetite			65	

Supplemental Table S5. Calculated distribution of Fe among reaction products in experiment OlivOpx230 (all data given in mmoles per g total solids).

Experiment	Duration (h)	pH in situ [#]	% overall reaction	% olivine reacted	% olivine reacted per hour	Source
OlivOpx230	9287	8.8	53	45	-	This study
OlivOpx230med	2709	7.2	1.9	1.4 [*]	0.0005	This study
<i>Olivine only experiments:</i>						
Oliv230	8159	7.7	4.9	4.9	0.0006	McCollom et al. (2016)
Oliv230pH	2972	9.3	70	70	0.0235	McCollom et al. (2020)
Oliv230fine	4293	8.1	25	25	0.0058	McCollom et al. (2020)
<i>Estimated olivine reaction during stages of OlivOpx230:</i>						
Stage I-II	4000	7.8	-	2.1 [†]	0.0005	This study
Stage III	5278	8.8	-	42.9	0.0081 [‡]	This study

[#]Average in situ pH. ^{*}Estimated based on overall reaction percent, relative proportion of reactants, and the assumption that Opx reacts twice as fast as olivine per gram. [†]Estimated amount of olivine reacted after 4000 hours assuming that it reacted at the same rate observed for OlivOpx230med. [‡]Estimated rate of olivine reaction during Stage III (4000-9578 h of experiment).



Supplemental Figure S1. Schematic drawing of flexible-cell hydrothermal reaction system used in the experiments. The reactor lies horizontal in the furnace during operation. The initial volume of the internal gold reaction cells used in the experiments were 55-62 ml, but the volume decreased as the cell was squeezed down during initial pressurization and when fluids were removed during sampling.

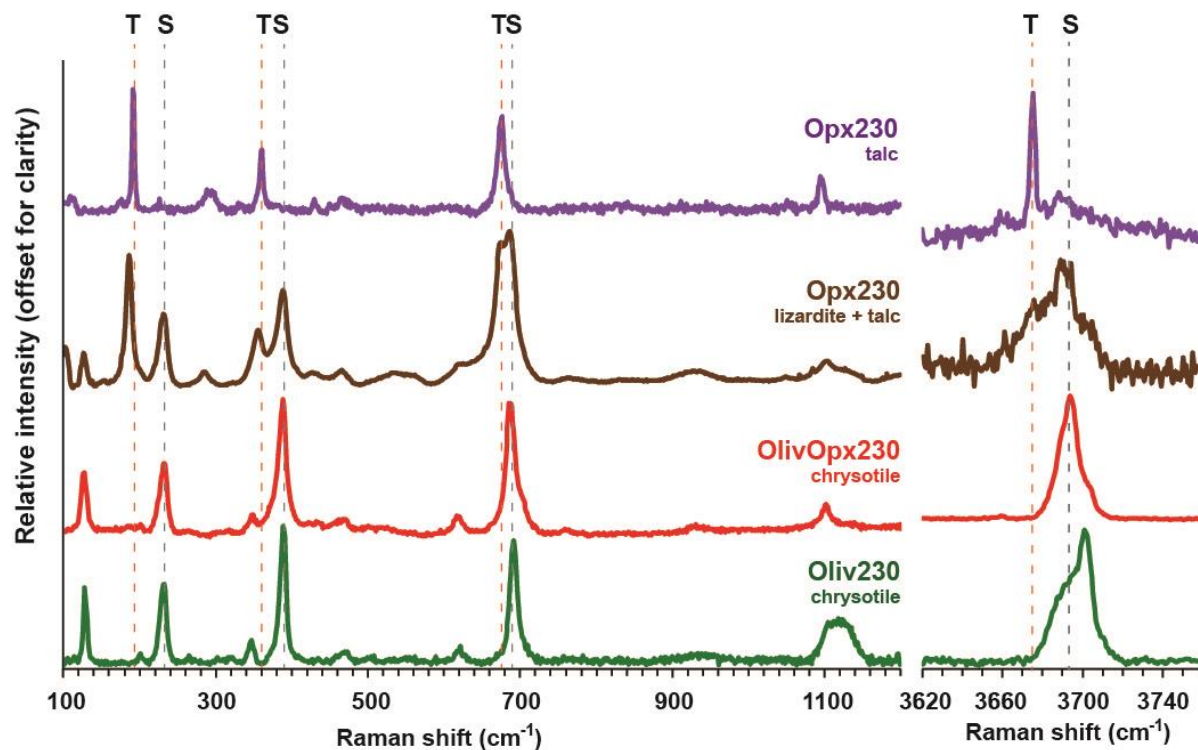


Figure S2. Raman spectra of experimental reaction products. Also shown for comparison is the Raman spectrum for chrysotile from an olivine-only experiment (Oliv230; McCollom et al., 2016). The bands designated by the gray dashed lines labelled “S” are attributed to serpentine minerals (lizardite or chrysotile) while the orange dashed lines labelled “T” identify peaks corresponding to talc. The shape of the OH stretching band at 3680-3720 cm⁻¹ is consistent with the lizardite structure in experiments Opx230, and with chrysotile in OlivOpx230 and Oliv230 (e.g., Petriglieri et al., 2015). The Raman spectrum for brucite crystals from OlivOpx230 is shown in Supplemental Figure S4.

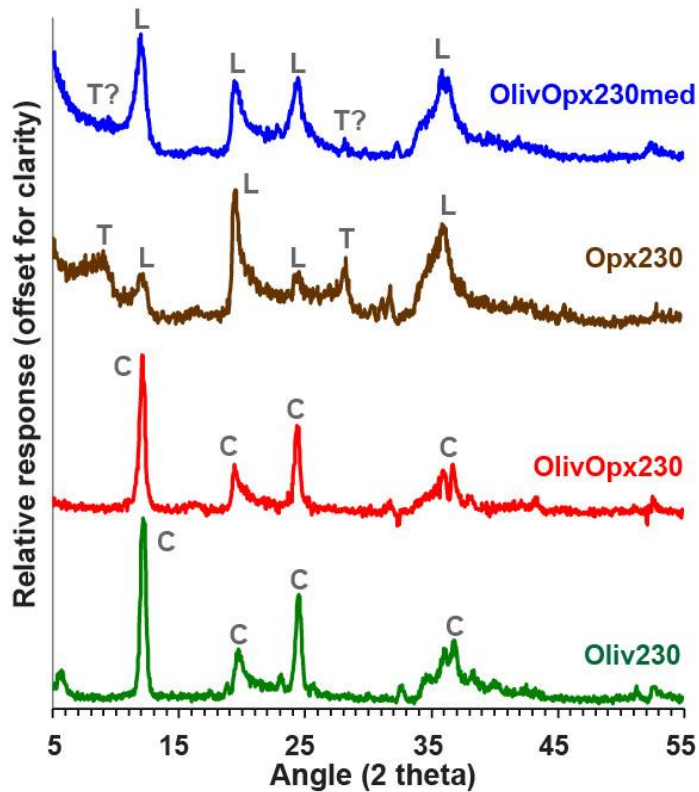
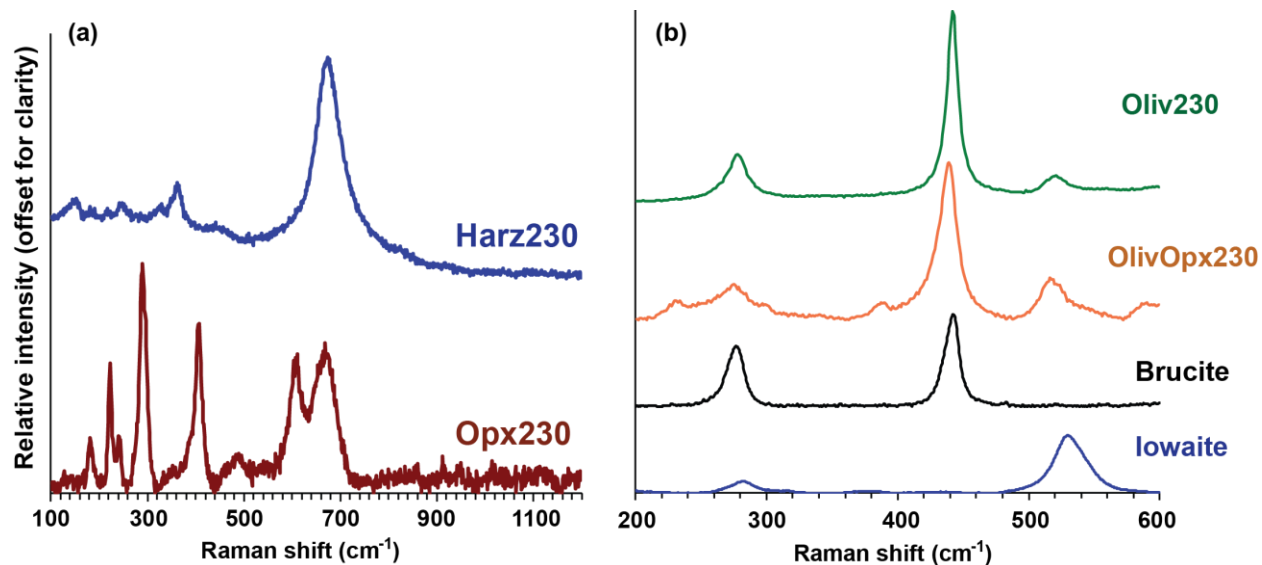
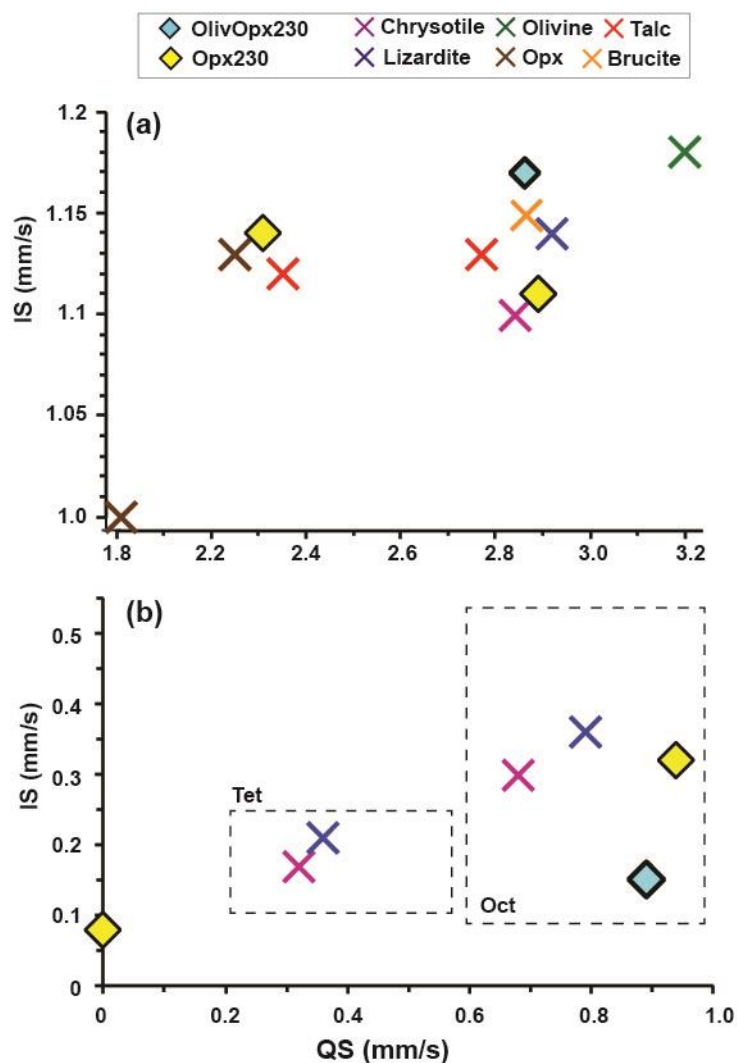


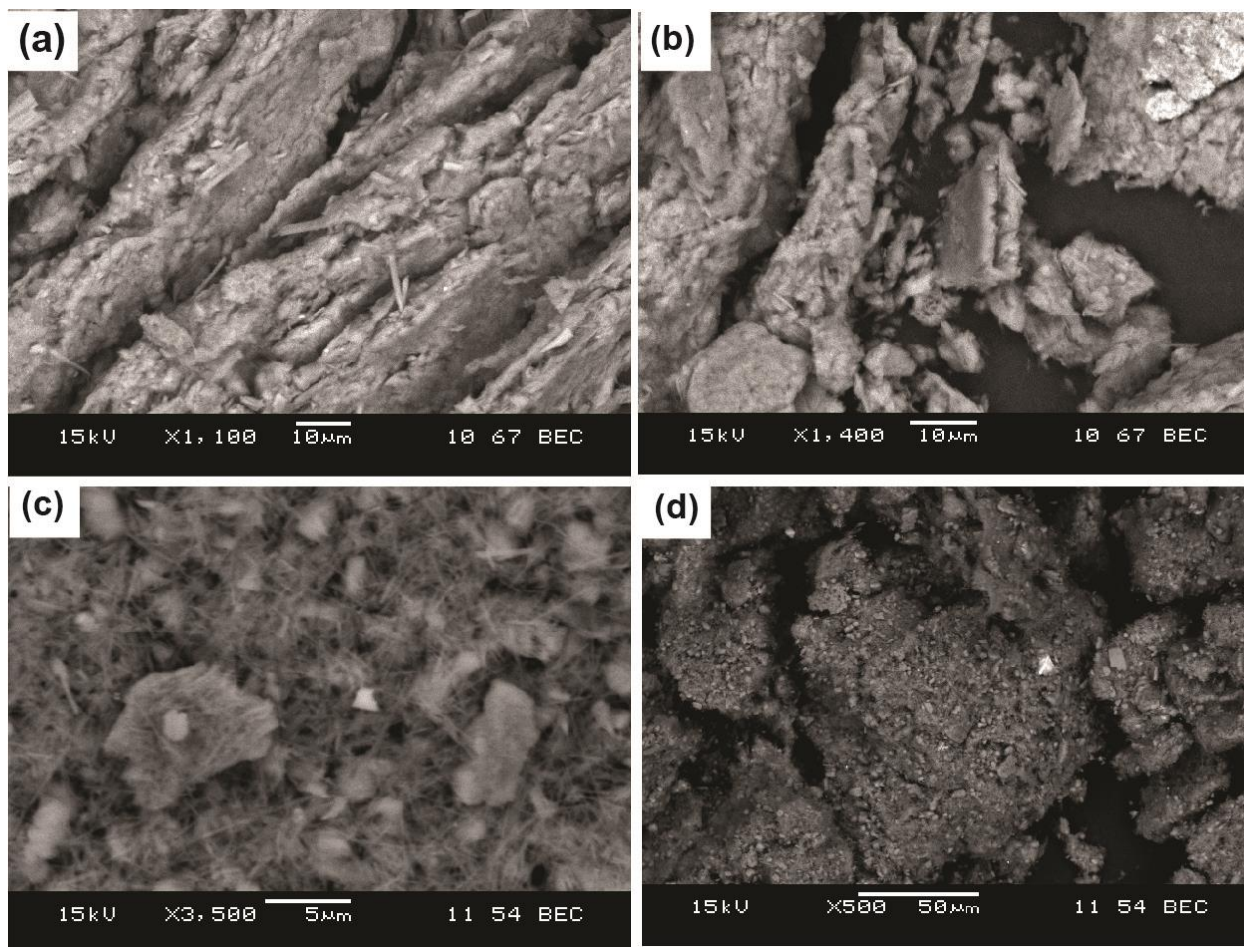
Figure S3. Results of X-ray diffraction analysis of reaction products. To focus on secondary silicates, the XRD analyses were performed on the fine-grained mineral fraction separated from the bulk fraction (see Detailed Methods above). Labels identify peaks attributed to lizardite (L), chrysotile (C), or talc (T). The variation in peak shapes for lizardite is likely attributable to variations in degree of crystallinity and fine-scale admixture of other phases.



Supplemental Figure S4. Additional Raman spectra from reacted solids. (a) Fe-oxide minerals from Opx230, identified as hematite. (b) Spectra for brucite crystals from OlivOpx230 and an olivine-only experiment (Oliv230; McCollom et al., 2016), with reference spectra for brucite and iowaite shown for comparison (from RRUFF database). The peak at ~ 520 cm⁻¹ in the OlivOpx230 and Oliv230 spectra is identified as iowaite that is intermixed with the brucite in the products of these experiments. The presence of iowaite is also supported by the observation of elevated Cl contents in many brucite crystals (see text and McCollom et al., 2016 for further details).



Supplemental Figure S5. Isomer shift (IS) versus quadrupole splitting (QS) from Mössbauer analysis of secondary silicates from the laboratory experiments, with parameters for several relevant minerals shown for reference (crosses; from Dyar et al., 2006). (a) Parameters corresponding to Fe^{II}. (b) Parameters corresponding to Fe^{III}. Dashed boxes outline parameters assigned to tetrahedral (Tet) or octahedral (Oct) sites for serpentine minerals. Mössbauer measurements were performed on secondary silicates separated from the bulk solids by sonication (see Detailed Methods).



Supplemental Figure S6. Example back-scattered images of solids obtained from the process used to separate secondary silicates from remaining reactant minerals for Mössbauer and XRD measurements. (a,b) From Opx230. (c,d) From OlivOpx230.

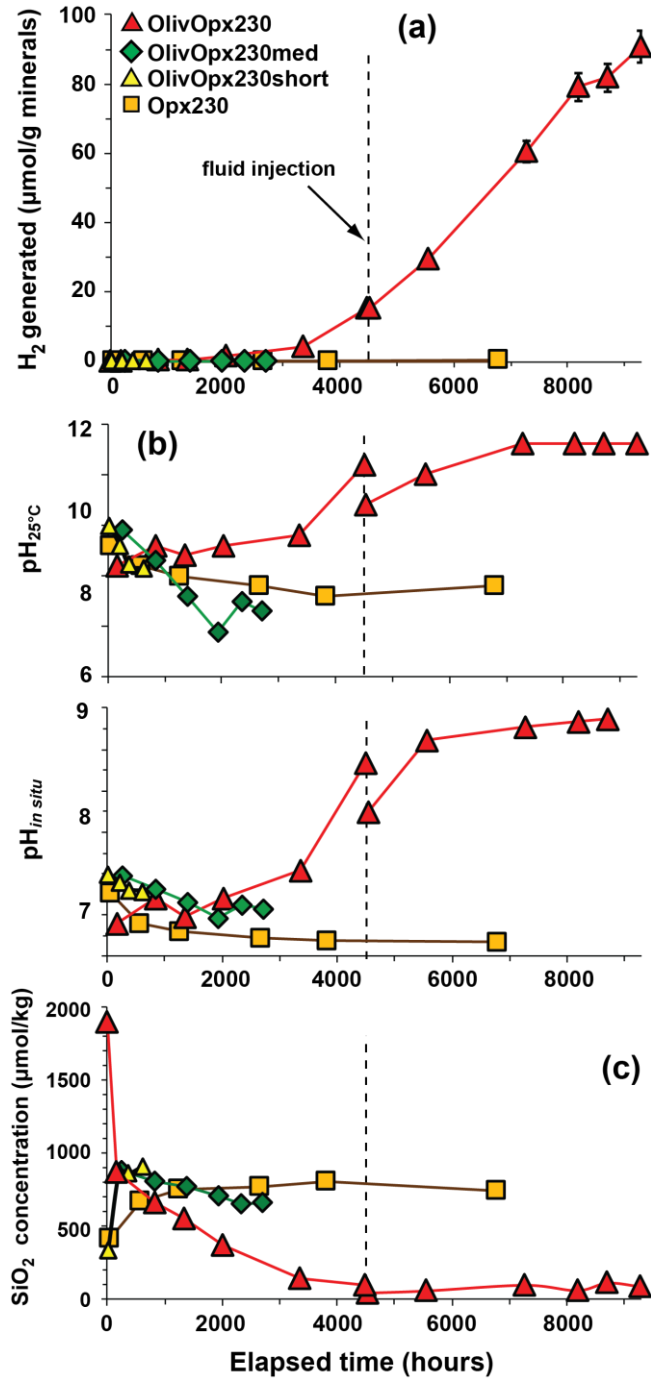
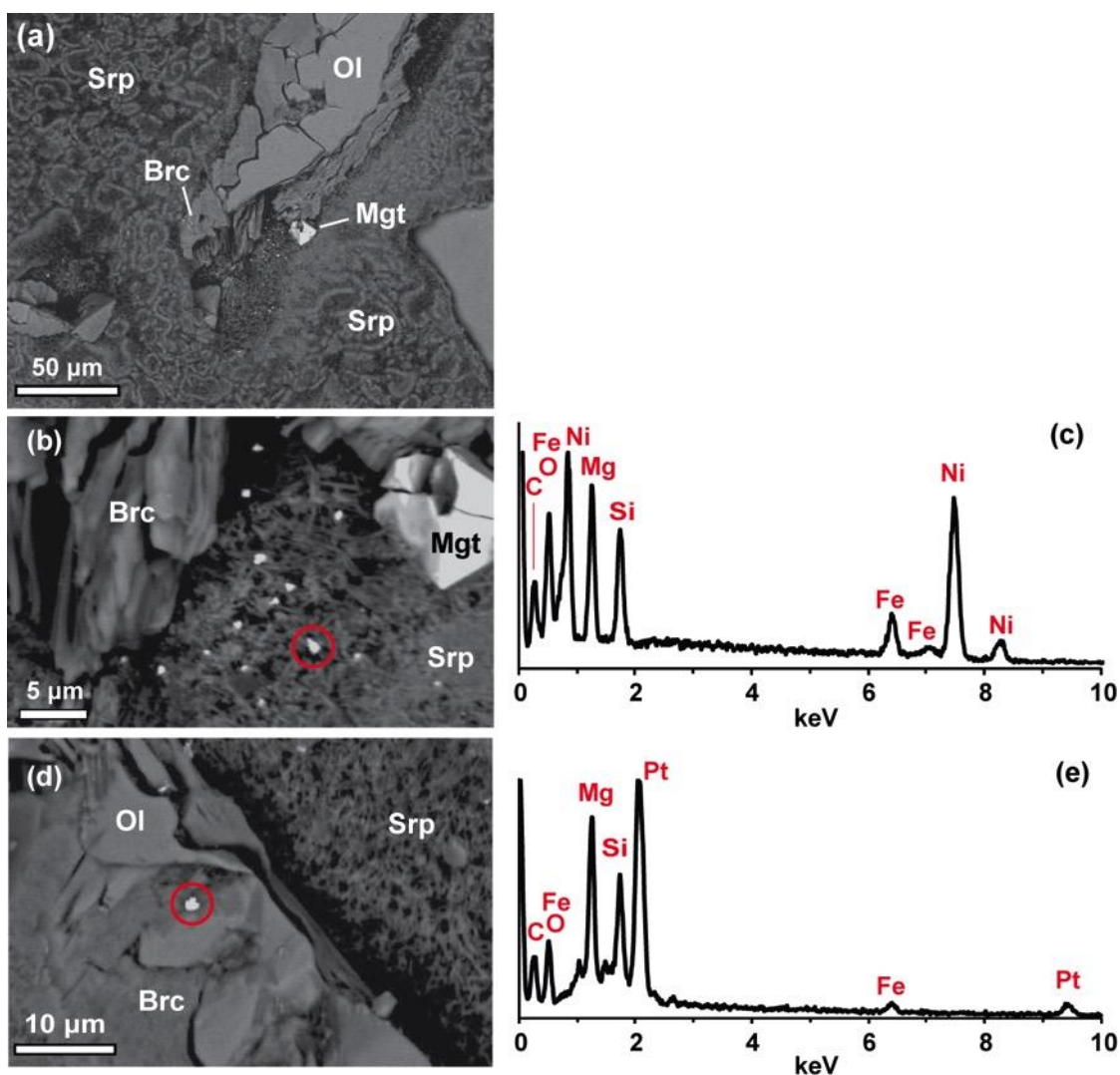
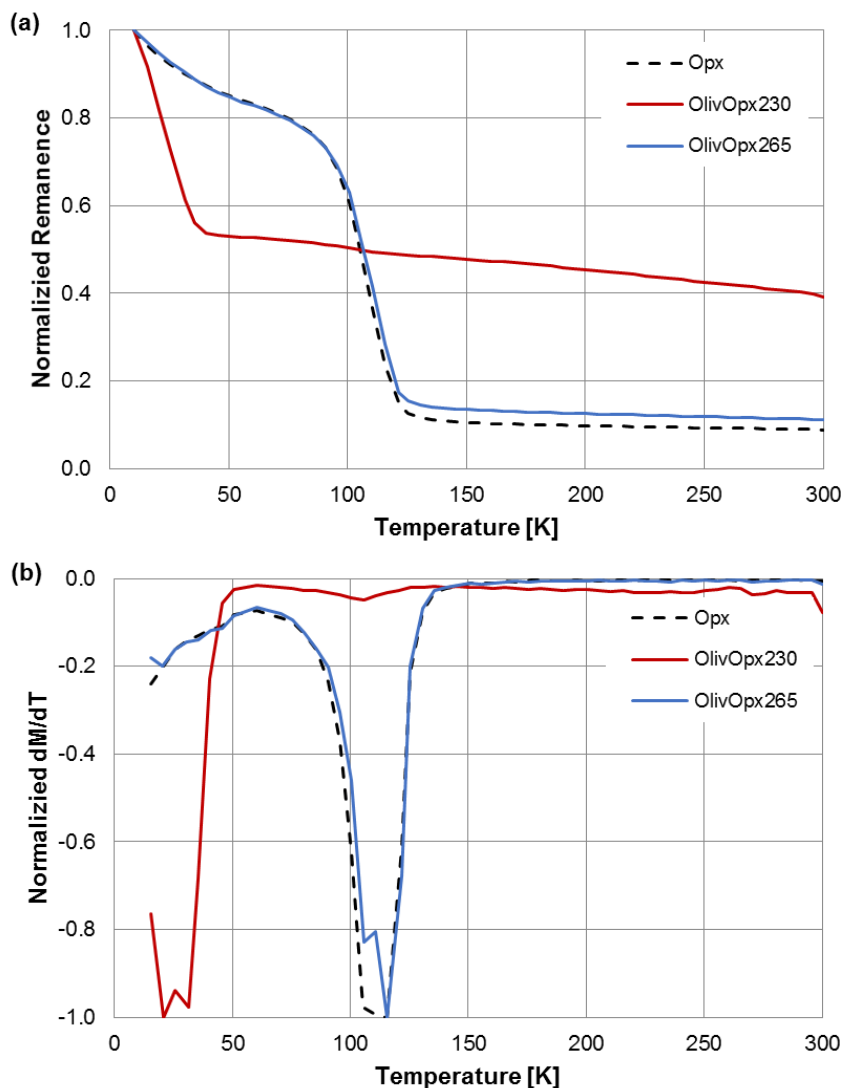


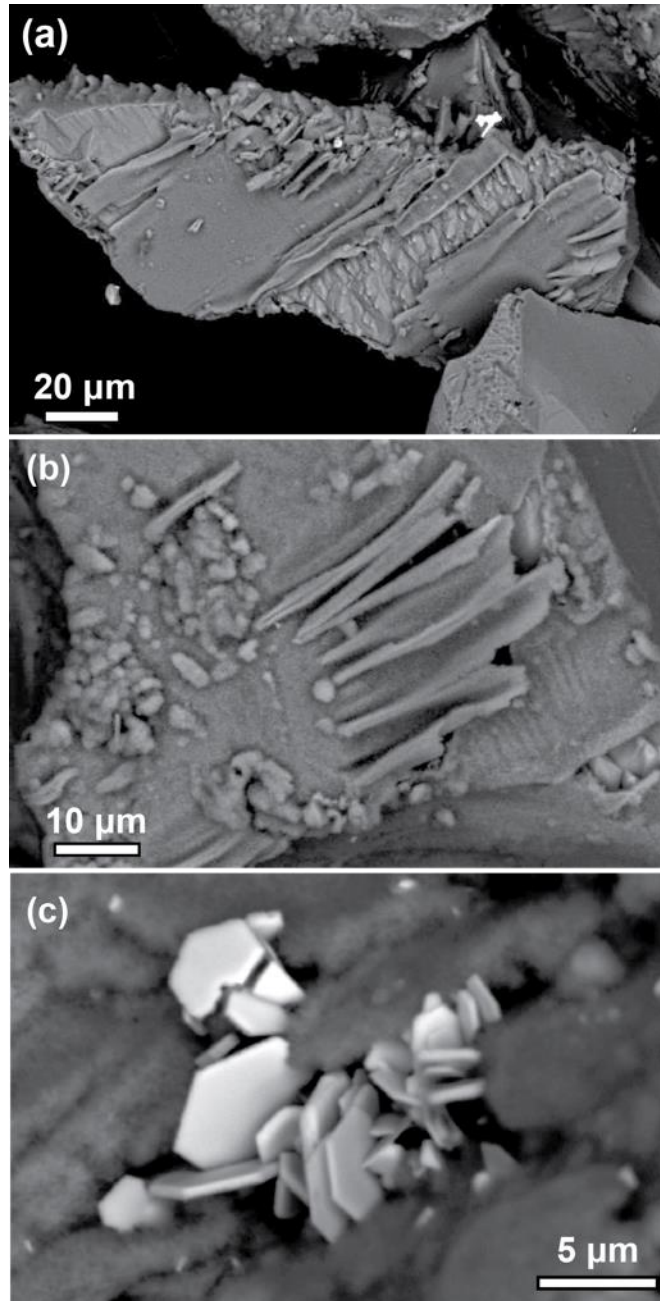
Figure S7. Fluid compositions during olivine plus Opx mixture experiments at 230 °C with data for Op_x230 shown for comparison. (a) Total amount of H₂ generated per g mineral reactant. (b) Measured room temperature pH (pH_{25°C}) and calculated in situ pH (pH_{in situ}). (c) Dissolved SiO₂ concentration. Vertical dashed lines indicate injection of additional fluid into experiment OlivOp_x230 at 4514 h. Except where shown, analytical errors are smaller than the symbols.



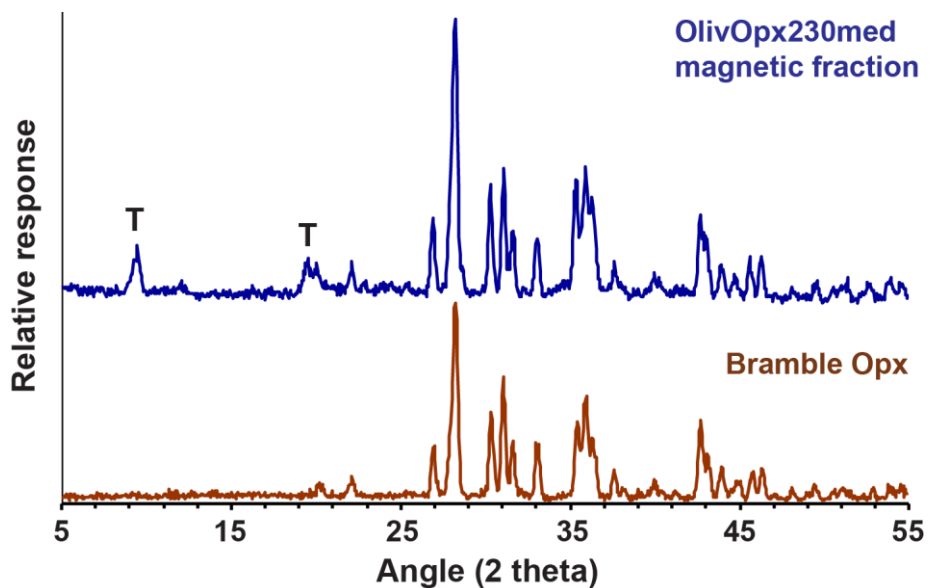
Supplemental Figure S8. Examples of apparent occurrences of native metals in experiment OlivOpx230. (a) Back-scattered SEM image showing overview of reaction products in polished grain mount. (b) Expanded view from (a), with EDS of area centered on bright particle outlined by the red circle shown in (c). The EDS is dominated by Ni and Fe with little O, indicating the small bright particles are composed of a Ni-Fe alloy. The Mg and Si in the EDS data are likely from serpentine surrounding the alloy particle. (d) Image of area at olivine-brucite interface, with EDS of area outlined by red circle shown in (e). The prominent Pt peak and lack of significant peaks for S or O indicates the bright particle in the circle is native Pt. Mineral abbreviations: Srp = serpentine (chrysotile), Brc = brucite, Ol = olivine, Mgt = magnetite.



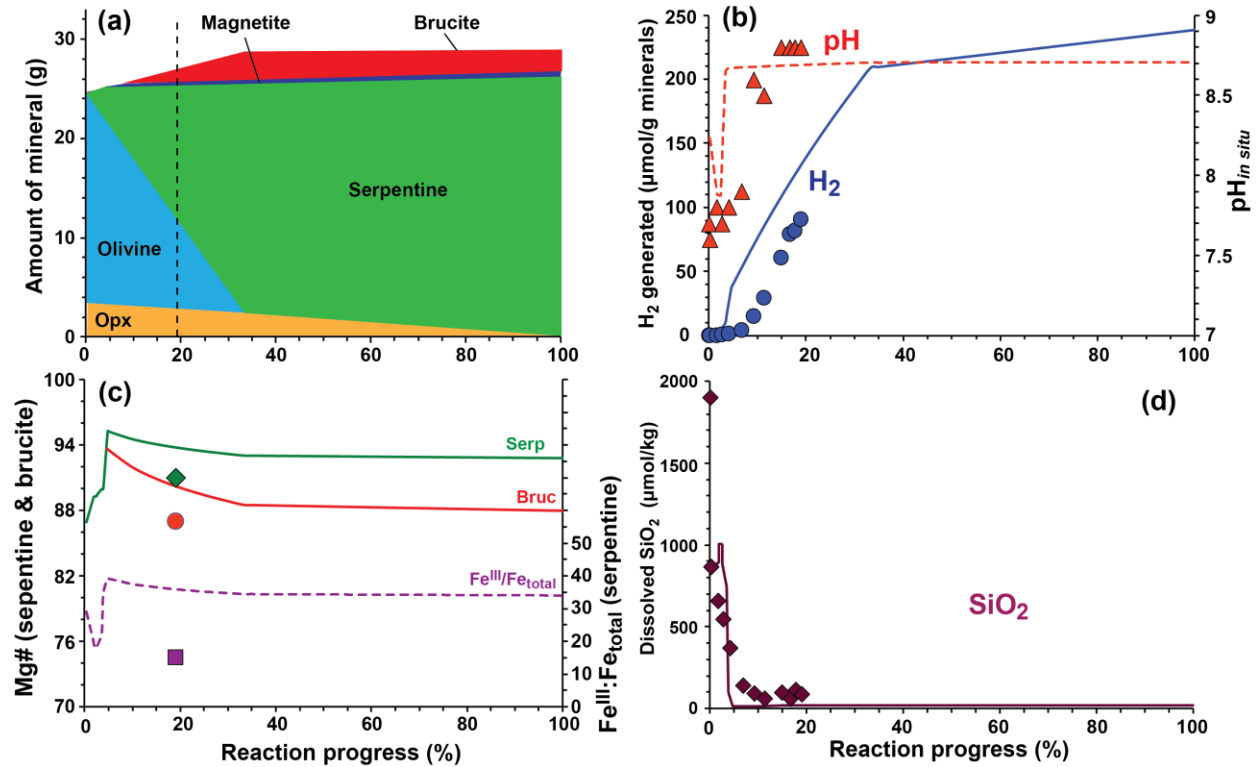
Supplemental Figure S9. (a) Normalized low-temperature remanence curves and their (b) temperature derivatives (dM/dT) for OlivOpx230, OlivOpx265 and Bamble Opx. Both types of curves are useful for identifying magnetic transition temperatures. A decrease in magnetization at $\sim 120\text{K}$ is characteristic of the Verwey transition for pure magnetite ($T_v=120\text{K}$) and is observed for OlivOpx265 and Opx. OlivOpx230 displays a transition near 30 K consistent with a cation substituted magnetite (e.g. titanomagnetite, Moskowitz et al., 1998) along with a weak inflection near 110K (easily seen in the derivative curve) indicating a small amount of nearly pure magnetite. Also, the gradual decrease in magnetization (particularly below 50 K where roughly 60% of the initial remanence has decayed) is characteristic of thermal unblocking associated with magnetic nanoparticles ($< 50\text{ nm}$). Remanence curves are normalized by their field-cooled saturation remanence values at 10 K and derivative curves are normalized by their maximum (negative) value.



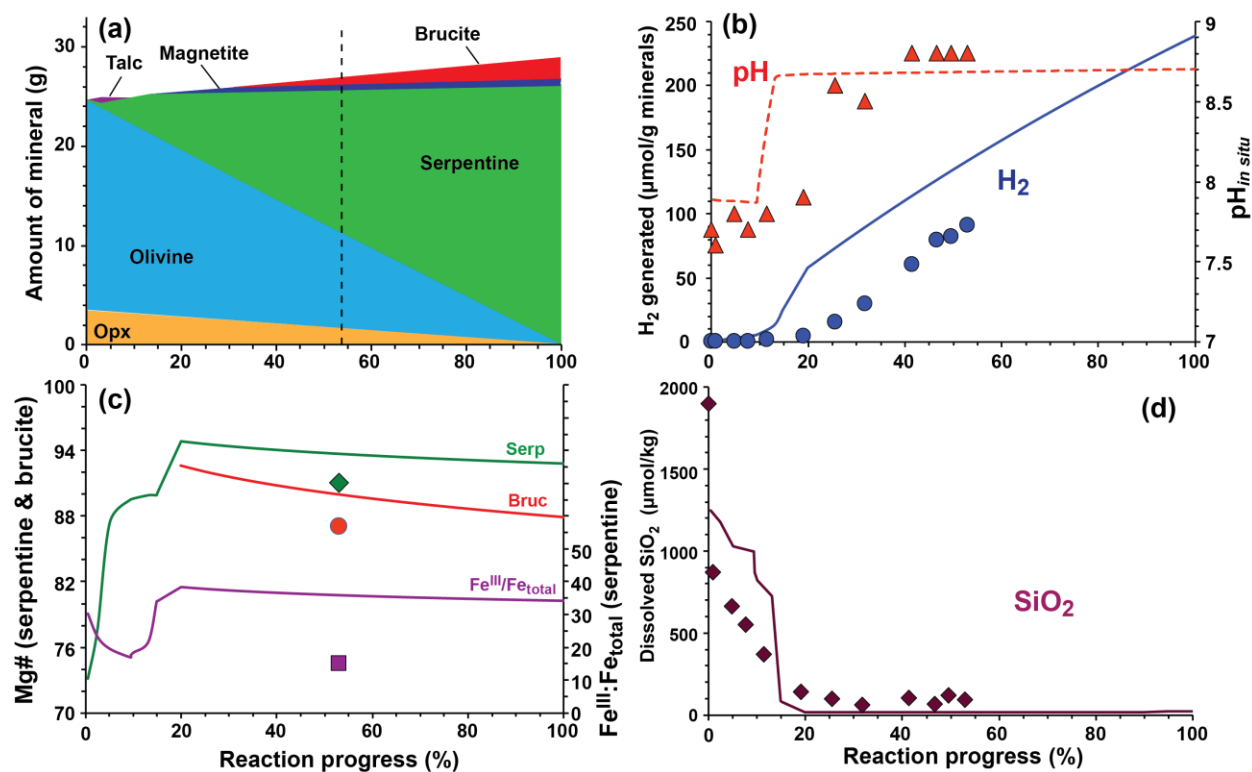
Supplemental Figure S10. Back-scattered electron images of representative reaction products from the short-term olivine plus Opx experiment (OlivOpx230short). (a,b) Rind of secondary products accumulated on surface of remnant reactant minerals. The underlying olivine is exposed in (a). In many areas, the thin rind is crinkled up to give a corrugated texture. (c) Hexagonal minerals embedded in alteration rind, presumably hematite.



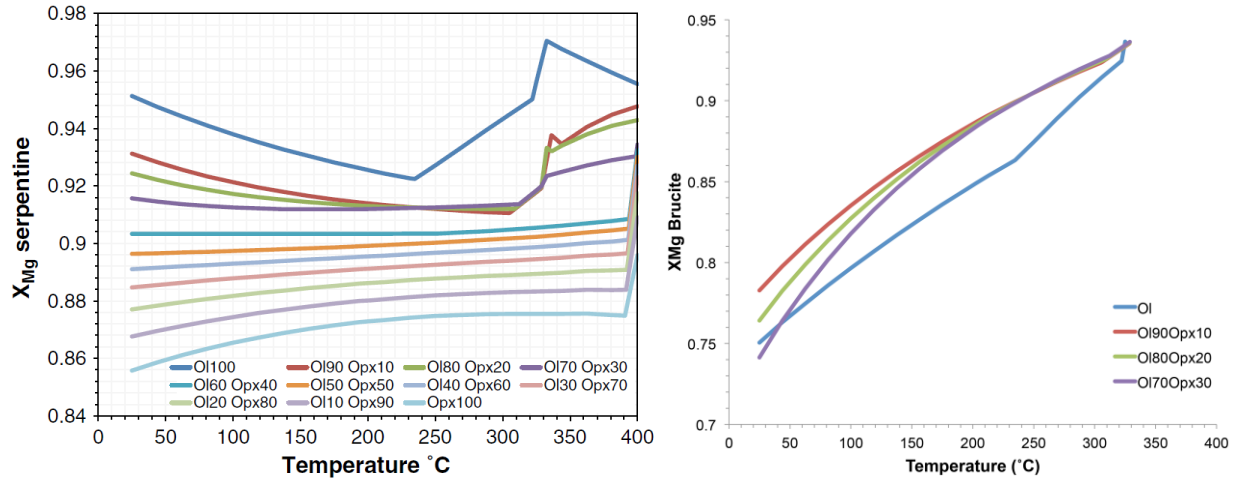
Supplemental Figure S11. X-ray diffraction pattern for magnetic particles removed from reaction products of experiment OlivOpX230med, with the diffraction pattern for unreacted OpX shown for comparison. Most of the peaks in the OlivOpX230med pattern can be attributed to unreacted OpX, but a couple of peaks are apparently attributable to talc (T). The other characteristic peak for talc at $2\theta = 28.7^\circ$ is not apparent owing to overlap with the peak for OpX.



Supplemental Figure S12. Results of a reaction path model for the case where olivine is allowed to react at a rate four times faster than Opx, consistent with the relative reactivities of these minerals for 230 °C based on the experiment results of Martin and Fyfe (1970). Selected results from OlivOpx230 shown for comparison (symbols). (a) Composition of solids as the reaction progresses, including reactants and secondary products. The dashed vertical line indicates the point in reaction progress where 53 wt% of the original reactant minerals have reacted as observed in OlivOpx230. (b) Predicted in situ pH and amount of H₂ generation. (c) Predicted Mg# of chrysotile and brucite, and the Fe^{III}:Fe_{total} ratio of chrysotile. (d) Concentration of total dissolved SiO₂. Trace amounts of tremolite are also predicted to precipitate during the early stages of the reaction path and is later replaced by calcite. However, the amounts of these minerals are too small to be shown in the diagram.



Supplemental Figure S13. Results of a reaction path model for the case where olivine and Opx are allowed to react at the same rate, with results of OlivOpX230 shown for comparison (symbols). (a) Composition of solids as the reaction progresses, including reactants and secondary products. The dashed vertical line indicates the approximate degree of reaction progress in OlivOpX230. (b) Predicted in situ pH and amount of H₂ generation. (c) Predicted Mg# of chrysotile and brucite, and the Fe^{III}:Fe_{total} ratio of chrysotile. (d) Concentration of total dissolved SiO₂. Trace amounts of talc and tremolite are also predicted to precipitate during the early stages of the reaction path and is later replaced by calcite. However, the amounts of these minerals are too small to be shown in the diagram.



Supplemental Figure S14. Predicted Fe contents in serpentine (left) and brucite (right) as a function of temperature during serpentinization of protoliths having distinct olivine:orthopyroxene mass ratios, as calculated by Klein et al. (2013). Calculations are performed for 50 MPa and a water:rock ratio near one. Left panel is Figure 9 of Klein et al. (2013). Figure in right panel is from the same model calculations, but was not shown in the published paper.